scientific reports

Check for updates

OPEN

Oxidative degradation of chitosan by Fe-MCM-41 heterogeneous Fenton-like system

Zhang Zhang[1], Wuheng Dong[2,3,4]✉ & Yongchun Huang[1,2,3,5]✉

We herein disclosed an efficient multiphase Fenton-like catalytic system for oxidative degradation of chitosan. By utilizing Fe-MCM-41, featured with regular mesoporous structure and high specific surface area, the activation efficiency of H_2O_2 was significantly enhanced and the chitosan degradation efficiency proved by 28.1% higher than the conventional system using H_2O_2 alone. Under optimized conditions (5 g/L chitosan, 0.5 g/L Fe-MCM-41, 0.16 mol/L CH_3COOH, 0.86 mol/L H_2O_2, 50 °C, 140 min), the viscosity reduction rate of chitosan reached an impressive 98.2%. Among the catalysts tested, Fe-MCM-41 with a loading factor of x = 0.12 demonstrated optimal degradation performance. After four recycles, the degradation efficiency maintained > 93.6%, demonstrating its excellent stability and recyclability for potential industrial applications. Kinetic studies provided further elucidation of the reaction mechanism, which indicated that the degradation process of chitosan followed a first-order kinetic model, with an apparent activation energy (E_a) of 48.91 kJ/mol. This novel and efficient strategy for chitosan degradation, addressed the challenges of catalyst recovery and secondary pollution typically associated with traditional Fenton systems, and posed broad application potential for polysaccharide material processing.

Keywords Molecular sieve, Catalyst, Fe-MCM-41, Fenton-like

Chitosan, a natural polysaccharide derived from partial deacetylation of chitin, has found broad application in medicine, food, and agriculture sciences owing to its excellent biocompatibility and renewability[1,2]. However, the high molecular weight and dense crystalline structure make it poorly soluble, thus limit its wider applications. Consequently, the development of efficient methods for chitosan degradation has become increasingly attractive. In areas such as plastic alternatives, biomedicine, and functional materials, oligochitosan, a degradation product of chitosan, has attracted significant attention due to its superior water solubility and bioactivity[3,4]. Therefore, the search for efficient and controllable degradation methods are highly desirable target of ongoing research.

Among the various degradation techniques, chemical oxidation—particularly methods using hydrogen peroxide—has been widely applied due to its high reaction efficiency[5]. For example, Ding et al.[6] investigated the oxidative degradation of chitosan using hydrogen peroxide under various pH and temperature conditions, and proposed the corresponding degradation mechanism. Similarly, Chen et al.[7] successfully degraded chitosan via hydrogen peroxide, yielding low-molecular-weight, water-soluble chitosan. Nevertheless, the use of H_2O_2 alone for chitosan degradation is still challenging in terms of low efficiency and poor controllability over the degree of degradation.

To enhance the degradation efficiency of chitosan, researchers have sought to incorporate iron ions, thereby constructing a Fe^{3+}/H_2O_2 Fenton-like homogeneous degradation system. Chu et al.[8] demonstrated that the Fe^{3+}/H_2O_2 system remarkably improved the degradation efficiency of chitosan than using H_2O_2 alone. Nonetheless, this system continues to encounter some challenges, including difficult catalyst recovery, secondary pollution by residual iron ions, and a narrow applicable pH range, which restricts its industrial applications. Therefore, an urgent need exists formore efficient, environmentally friendly, and easily recoverable protocol to address these challenges.

Mesoporous materials have recently been extensively utilized in multiphase Fenton-like catalytic systems, owing to their high specific surface area, tunable pore sizes, and exceptional structural stability[9–11]. MCM-41,

[1]School of Biological and Chemical Engineering, Guangxi University of Science and Technology, Liuzhou 545000, China. [2]Guangxi Key Laboratory of Green Processing of Sugar Resources, Guangxi University of Science and Technology, Liuzhou 545000, China. [3]Guangxi Liuzhou Luosifen Engineering Technology Research Center, Guangxi University of Science and Technology, Liuzhou 545000, China. [4]Laboratory of Drug Design and Synthesis, Medicine Center, Guangxi University of Science and Technology, Liuzhou 545006, Guangxi, China. [5]Guangxi Vocational and Technical College, Nanning 530026, China. ✉email: dongwuheng405@126.com; huangyc@yeah.net

characterized by its moderate pore size, high surface area, and relatively straightforward preparation process, has emerged as an ideal carrier for metal ions[12]. In comparison to SBA-15 and MCM-48, MCM-41 shows superior performance in mass transfer processes, especially after loading with iron ions, thereby significantly enhancing its catalytic efficiency. The utilization of Fe-MCM-41 (iron-loaded MCM-41) in multiphase Fenton-like catalysis has been thoroughly investigated and its high catalytic efficiency for hydrogen peroxide activation has been validated. For instance, Deng et al.[13] demonstrated that the Fe-MCM-41 catalytic system could efficiently degrade methylene blue dye within 120 min. Liang et al.[14] revealed that this material could almost completely degrade Rhodamine B within 30 min. These studies underscore that Fe-MCM-41 can effectively facilitate the decomposition of H_2O_2, generating hydroxyl radicals ($^{\cdot}OH$) and thus achieving efficient degradation of organic pollutants.

Considering the outstanding performance of Fe-MCM-41 in the degradation of organic pollutants, it is postulated that this material also possesses significant potential for the degradation of chitosan. The pore size of Fe-MCM-41 is optimal for the unobstructed passage of hydrogen peroxide molecules, and the iron ions within and around the pores efficiently catalyze H_2O_2 decomposition, producing $^{\cdot}OH$ radicals. These radicals react rapidly with chitosan, facilitating its efficient degradation[15–17]. As a heterogeneous catalyst, Fe-MCM-41 is easy to recover, significantly reducing the risk of secondary pollution from residual iron ions, and demonstrates exceptional catalytic stability and reusability over extended use. Consequently, Fe-MCM-41 is regarded as an ideal catalytic material for the degradation of chitosan.

This study aims to establish an efficient multiphase Fenton-like catalytic system for the oxidative degradation of chitosan by optimizing the iron loading, reaction conditions, and recyclability of Fe-MCM-41. The research focuses on key parameters, including iron loading, H_2O_2 concentration, and reaction temperature on the degradation efficiency. In addition, the study explores the kinetic characteristics of the Fe-MCM-41 Fenton-like system in chitosan degradation and its catalytic mechanism for the decomposition of H_2O_2. By systematically evaluating the activity and stability of the catalyst under different reaction conditions, its feasibility in practical applications is further revealed.

Compared with traditional homogeneous Fenton systems and other catalytic systems, Fe-MCM-41 exhibits obvious advantages in catalytic efficiency, catalyst recyclability, and stability. After four cycles of reuse, the optimized Fe-MCM-41 system retained a degradation efficiency more than 93.6%, showing outstanding stability and reusability. At the same time, the research results show that the degradation process of chitosan conforms to the first-order reaction kinetic model, and its catalytic mechanism is explained in detail. This multiphase Fenton-like catalytic system effectively solves the problems of residual iron ions and secondary pollution in traditional systems, showing its broad prospects in industrial applications.

In conclusion, this study presents an efficient and environmentally friendly multiphase Fenton-like catalytic system that not only offers a new solution for the industrial application of chitosan but also paves the way for advancements in biomedicine and functional materials.

Materials and methods

Experimental apparatus

HK-1D Thermostatic Water Bath, Nanjing WuHua Intelligent Equipment Co., Ltd; OS-20-Pro Mechanical Stirrer, Beijing Dragon Instrument Co., Ltd; DF-101S Collecting Magnetic Stirrer, XinNiu Technology Co., Ltd; Ubbelohde Viscometer (0.57 mm), Shanghai LiangJing Glass Instrument Factory; Explosion-proof Stainless Steel Reactor, XinNiu Technology Co., Ltd; SHZ-DIII Circulating Water Vacuum Pump, Shanghai JinFu Laboratory Instrument Equipment Co., Ltd; JS-510 Mechanical Stopwatch, Shanghai Star Diamond Stopwatch Co., Ltd; DHG-9053A Electric Thermostatic Drying Oven, Shanghai YiHeng Scientific Instrument Co., Ltd; Nabertherm GmbH Muffle Furnace, Nabertherm GmbH, Germany; BS224 S Analytical Balance, Sartorius AG, Germany; Rigaku Dmax-rA X-ray Diffractometer, Rigaku Corporation, Japan; ZSX Primus III + X-ray Fluorescence Spectrometer, Rigaku Corporation, Japan; ZEISS Sigma 300 Scanning Electron Microscope, Carl Zeiss AG, Germany; Micromeritics ASAP 2460 Surface Area and Pore Size Analyzer, Micromeritics Instrument Corporation, USA; Malvern Zetasizer Nano ZS90, Malvern Instruments Ltd.; TG 209 F1 Libra Netzsch, Germany; Avatar 360 infrared spectrometer, Nicolet, USA.

Experimental reagents

Hexadecyltrimethylammonium bromide and tetraethyl orthosilicate: analytical grade, Tianjin Kermel Chemical Reagent Co., Ltd; Ferric nitrate nonahydrate: 98% purity, Energy Chemical Co., Ltd; Tartaric acid: 95% purity, Bide Pharmatech Ltd; Sodium hydroxide, 30% hydrogen peroxide, glacial acetic acid, and sodium acetate: analytical grade, Xilong Scientific Co., Ltd; Chitosan: industrial grade, 90% deacetylation, Shenzhen Zhongfayuan Biotechnology Co., Ltd.

Preparation of catalyst

Preparation of Fe-MCM-41[18,19]: First, ferric nitrate nonahydrate ($Fe(NO_3)_3{\cdot}9H_2O$, as an iron source) and tartaric acid (TA) were dissolved in deionized water and stirred at room temperature for 40 min to ensure that the solution was fully mixed. Subsequently, cetyltrimethylammonium bromide (CTAB, acting as a template agent) was added and stirred for an additional 60 min until completely dissolved. Tetraethyl orthosilicate (TEOS, serving as the silica source) was then slowly added dropwise while stirring for 60 min to uniformly disperse the silicon source. Then, the pH was adjusted to 9–10 with sodium hydroxide (NaOH) solution and stirred for 4 h to generate the precursor of Fe-MCM-41.

Subsequently, the resulting solution was then transferred into a stainless-steel autoclave lined with polytetrafluoroethylene (PTFE) and subjected to crystallization at 110 °C for 72 h to form a stable mesoporous structure. After crystallization, the mixture was cooled to room temperature, and the solid product was isolated

via vacuum filtration. The solid was thoroughly washed with deionized water until the filtrate reached a pH of 7.0. The isolated solid was then dried overnight at 100 °C to remove any residual moisture. Finally, the dried sample was calcined in a muffle furnace, with the temperature gradually increased at 5 °C/min to 550 °C and held for 6 h to remove the template agent, ultimately yielding Fe-MCM-41 molecular sieves.

Fe-MCM-41 samples with varying iron contents were synthesized by adjusting the molar ratio of the reactants (1.0 SiO_2: 0.2 CTAB: x Fe^{3+}: 100 H_2O, where x = 0.04, 0.08, 0.12, and 0.16), designated as 0.04-Fe-MCM-41, 0.08-Fe-MCM-41, 0.12-Fe-MCM-41, and 0.16-Fe-MCM-41, respectively. As a control, MCM-41 was synthesized using the same method but without an iron source, yielding a pure silica MCM-41 sample.

Analysis of catalyst

X-ray diffraction (XRD) analysis

The crystal structure of the catalyst was characterized using X-ray diffraction with Cu Kα radiation, scanning from 0.5° to 10° for low angles and 10° to 80° for wide angles. This analysis confirmed the mesoporous structure of Fe-MCM-41 and assessed the effect of iron ion incorporation on the structure.

Specific surface area and pore size (BET) analysis

The catalyst's specific surface area was measured using the BET method, and the pore size distribution was analyzed using the BJH method. Before analysis, the sample was vacuum-treated at 300 °C for 6 h. BET analysis examined the pore structural characteristics of Fe-MCM-41.

Scanning electron microscopy (SEM) analysis

The surface morphology of the catalyst was observed using a scanning electron microscope. The samples were sputtered with gold for 45 s on a Quorum SC7620 sputter coater at an accelerating voltage of 3 kV. SEM analysis was used to evaluate the particle distribution of Fe-MCM-41.

Fourier transform infrared (FT-IR) spectroscopy analysis

Catalyst samples were analyzed using an Avatar 360 FT-IR spectrometer. KBr pellets were prepared, and measurements were taken across a range of 4000–400 cm^{-1}.

X-ray fluorescence (XRF) analysis

The iron content in the catalyst was quantified using XRF, covering an analysis range from 9Na to 92U, to assess the distribution of iron in the catalyst.

Thermogravimetric analysis (TGA)

Catalyst samples were analyzed using a TG209F1 Libra thermogravimetric analyzer. Air was used as the reactive gas, with the temperature raised from room temperature to 1000 °C at a rate of 10 °C/min.

Zeta potential analysis

The surface charge characteristics of the samples were determined using a Zeta potential instrument under different pH conditions. Zeta potential analysis was used to evaluate the dispersibility and stability of the catalyst in the aqueous phase.

Evaluation of catalyst activity

A specified amount of catalyst, chitosan and deionized water were added to a round-bottom flask and mechanically stirred in a constant temperature water bath for 30 min to reach adsorption equilibrium. Then acetic acid and H_2O_2 were added, and samples were taken after the reaction. The samples were diluted and centrifuged for detection and analysis. All experiments were conducted in triplicate, and the experimental results were taken as the average of three measurements. The stirring rate was set at 300 rpm, and the reaction temperature was controlled between 30 and 60 °C.

Analytical methods

Weigh an appropriate amount of chitosan and dissolve it in an acetic acid (0.2 mol/L)—sodium acetate (0.1 mol/L) buffer solution, stirring until the chitosan is completely dissolved to prepare the chitosan solution before degradation. The concentration of this solution should be prepared according to the experimental requirements and used for viscosity measurement as a benchmark before degradation.

After the degradation reaction is completed, a certain amount of the reaction solution is taken and diluted with the same buffer solution to keep the concentration of the diluted sample consistent with that of the chitosan stock solution before degradation. Subsequently, the diluted reaction solution is centrifuged to remove the solid precipitate, and the supernatant is taken as the chitosan solution after degradation for subsequent viscosity measurement.

Viscosity measurements were taken using an Ubbelohde viscometer under constant temperature conditions (30 ± 0.1 °C). The outflow time (t) of the pre-degradation chitosan stock solution and the degraded chitosan solution was recorded. Additionally, the outflow time (t_0) of the buffer solution used to prepare the chitosan solutions was measured as a baseline reference. The intrinsic viscosity of the chitosan solution, before and after degradation, was calculated using the empirical formula of the one-point method, as shown below[20–22]:

$$[\eta] = \frac{\eta_{sp} + 3\ln\eta_r}{4C}$$

figure: $\eta_r = \frac{t}{t_0}$, "η_r" is defined as the relative viscosity;$\eta_{sp} = \eta_r - 1$, "η_{sp}" is identified as the incremental viscosity ; "C" represents the concentration of the chitosan solution, expressed in g/mL.

The effectiveness of chitosan oxidative degradation was evaluated based on the rate of decrease in intrinsic viscosity, $[\eta]_r$, calculated as follows:

$$[\eta]_r\,(\%) = \frac{\eta_0 - \eta_t}{\eta_0} \times 100$$

In the formula: "η_0" represents the intrinsic viscosity of the chitosan solution before degradation; "η_t" represents the intrinsic viscosity of the chitosan solution after degradation.

Results and discussion

Characterization and analysis of the catalyst

X-ray diffraction (XRD) analysis of the catalyst

Figure 1 shows the X-ray diffraction (XRD) patterns of Fe-MCM-41 with varying iron contents (x Fe^{3+}): SiO_2, where x = 0.04, 0.08, 0.12, and 0.16). Figure 1a shows the XRD patterns of the catalyst in the low-angle range of 0.5° to 10°. At x = 0.04, the synthesized molecular sieve shows a well-defined XRD pattern with a sharp and intense (100) diffraction peak, as well as (110) and (200) peaks, indicating a highly ordered hexagonal arrangement and significant crystallinity[23]. As the iron content increases to x = 0.08 and x = 0.12, the intensity of all diffraction peaks slightly decreases, but the (100), (110), and (200) peaks remain clearly visible. This suggests that the mesoporous structure of the molecular sieve retains the hexagonal symmetry of MCM-41, despite a slight decrease in structural order[24]. However, at x = 0.16, Fe-MCM-41 shows a significant decrease in the intensity of the (100) peak, with the (110) and (200) peaks nearly disappearing. This indicates that the introduction of a large amount of iron disrupts the hexagonal symmetry of MCM-41 and partially disturbs the mesoporous structure. Excess iron may exist on the surface of the molecular sieve in the form of highly dispersed Fe_2O_3.

Figure 1b shows the X-ray diffraction (XRD) patterns of the catalyst in the wide-angle range of 10° to 80°. All four samples display characteristic SiO_2 diffraction peaks around 22°, consistent with SiO_2 as the primary component of the samples[25]. As the iron content increases, the intensity of the characteristic SiO_2 diffraction peak gradually diminishes. At x = 0.04, no iron oxide diffraction peaks are observed, suggesting that the introduced iron is highly dispersed within the MCM-41 framework. At x = 0.08, the Fe-MCM-41 sample shows a Fe_2O_3 diffraction peak at 2θ = 35.9°. At x = 0.12, a distinct Fe_2O_3 diffraction peak is observed at 2θ = 40.6°. At x = 0.16, the Fe-MCM-41 sample shows clear Fe_2O_3 diffraction peaks at 2θ = 33.2° and 40.8°[26]. These results suggest that in the range of x = 0.08 to 0.16, Fe is partially dispersed within the MCM-41 framework and partially exists as Fe_2O_3. As the iron content increases, the intensity of the Fe_2O_3 peaks increases, likely due to excess iron forming highly dispersed Fe_2O_3 on the surface of the molecular sieve. This observation is consistent with the XRD patterns observed in the low-angle range.

To investigate the effect of varying Fe content on the crystallite size of Fe_2O_3 in Fe-MCM-41, the Scherrer equation was used to estimate crystallite size. The formula is: $D = \frac{K \cdot \lambda}{\beta \cdot \cos\theta}$, where "D" is the crystallite size (nm), "λ" is the X-ray wavelength, "β" is the full width at half maximum (FWHM) of the diffraction peak (in radians), and "θ" is half of the diffraction angle (in radians). Using this formula, the Fe_2O_3 crystallite sizes for the 0.08-Fe-MCM-41, 0.12-Fe-MCM-41, and 0.16-Fe-MCM-41 samples were calculated. The results are presented in Table 1.

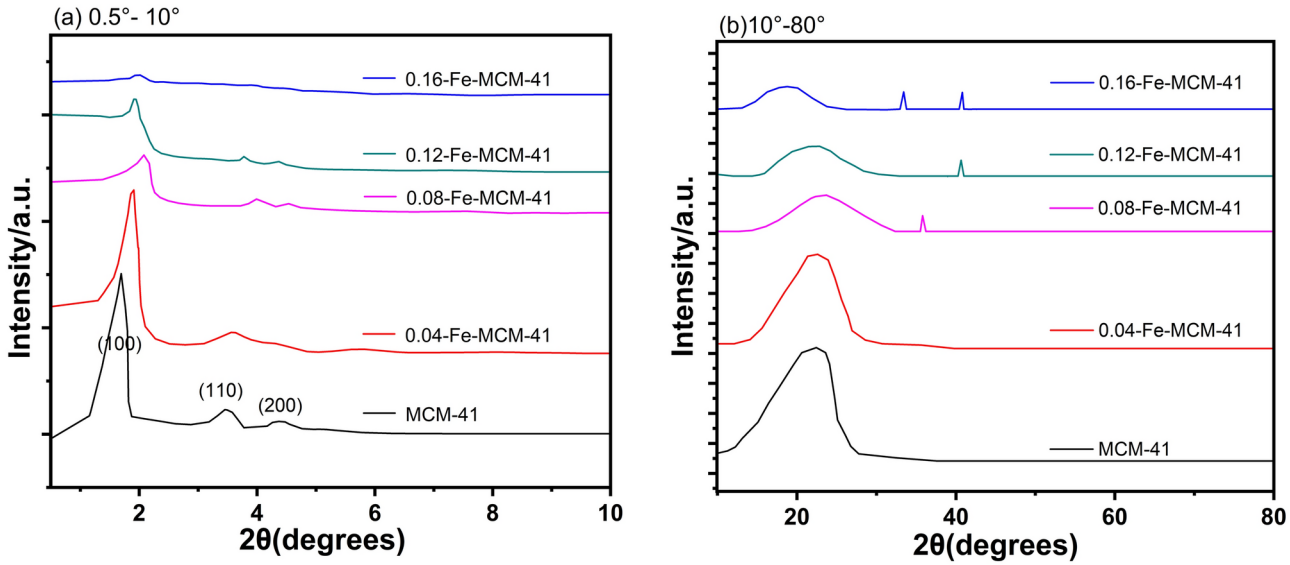

Fig. 1. XRD Patterns of MCM-41 and Fe-MCM-41 with varying Iron Contents (x = 0.04, 0.08, 0.12, 0.16).

Sample	2θ (°)	β (°)	D (nm)
0.08-Fe-MCM-41	35.9	0.398	20.98
0.12-Fe-MCM-41	40.6	0.401	21.12
0.16-Fe-MCM-41	33.2	0.384	21.59
0.16-Fe-MCM-41	40.8	0.366	23.16

Table 1. Crystallite sizes of Fe_2O_3 in Fe-MCM-41 samples with varying Fe Contents.

Sample	d_{100} (nm)	a_0 (nm)	Pore size (nm)	Wall thickness (nm)	Bet surface area $(m^2\,g)^{-1}$	Pore volume $(cm^3\,g)^{-1}$
MCM-41	5.21	9.03	3.65	5.38	932.69	0.81
0.04-Fe-MCM-41	4.63	8.01	3.61	4.40	801.46	0.96
0.08-Fe-MCM-41	4.25	7.35	3.54	3.81	715.78	0.96
0.12-Fe-MCM-41	4.54	7.85	3.06	4.79	665.71	0.90
0.16-Fe-MCM-41	4.38	7.57	2.67	4.90	350.28	0.64

Table 2. Physical parameters of Fe-MCM-41 with varying Iron Contents.

The results indicate that the Fe_2O_3 crystallite size increases as Fe content rises. For samples with lower Fe content (x = 0.08 and 0.12), the crystallite sizes were 20.98 nm and 21.12 nm, respectively, showing minimal variation and suggesting good dispersion of Fe species within the MCM-41 pores. However, at x = 0.16, the crystallite size significantly increased, reaching 21.59 nm and 23.16 nm, indicating a tendency for Fe_2O_3 particle agglomeration. This increase in crystallite size may reduce catalytic activity, as larger particles decrease the specific surface area[27]. Therefore, optimizing Fe content is crucial for maintaining the efficiency of the Fe-MCM-41 catalyst.

Specific surface area and pore size (BET) analysis

Table 2 summarizes the physical parameters of Fe-MCM-41 with varying iron loadings (x Fe^{3+}: SiO_2, where x = 0.04, 0.08, 0.12, and 0.16). The results indicate that as iron doping increases, the lattice constant, pore size, and specific surface area of Fe-MCM-41 gradually decrease. Notably, at higher iron content (x = 0.16), the specific surface area significantly decreases to 350.28 m^2/g, suggesting that the introduction of iron causes pore structure contraction and partial blockage[28]. The pore wall thickness initially decreases and then increases, indicating that the material's structure becomes looser at moderate iron content (x = 0.08), while at higher iron content, the pore walls become denser[29]. Although the pore volume shows minor fluctuations, it also decreases significantly at higher iron content.

The specific surface area is a critical factor in determining catalytic activity in multiphase Fenton-like reactions. A larger surface area provides more active sites, facilitating hydrogen peroxide (H_2O_2) decomposition and generating more hydroxyl radicals (·OH), thereby enhancing the catalytic reaction efficiency[30]. However, while increasing iron loading can enhance catalytic activity, excessive iron loading may cause pore blockage and a reduction in surface area, ultimately leading to decreased catalyst performance[31]. Therefore, optimizing iron content is crucial for balancing a large surface area with highly active iron sites.

Scanning electron microscopy (SEM) analysis

Figure 2 shows the scanning electron microscopy (SEM) images of Fe-MCM-41 with varying iron loadings (x Fe^{3+}: SiO_2, where x = 0.04, 0.08, 0.12, and 0.16). Slight nanoparticle agglomeration is observed, possibly due to the high energy, unsaturation, and instability of the mesoporous Fe-MCM-41 nanoparticles. During calcination, surface silicon hydroxyl groups of the nanoparticles underwent condensation reactions[32]. At x = 0.04, Fe-MCM-41 exhibits rod-like or spherical shapes with regular morphology and good structural order. At x = 0.08, Fe-MCM-41 primarily exhibits spherical shapes while maintaining good structural order. At x = 0.12, Fe-MCM-41 exhibits irregular nanoparticle block shapes alongside rod-like or spherical forms. At x = 0.16, Fe-MCM-41 predominantly exhibits irregular nanoparticle block shapes, indicating reduced structural order and hexagonal symmetry as Fe loading increases, consistent with the XRD results. These irregular nanoparticle blocks are inferred to be clusters of Fe_2O_3 oxides, based on the XRD results.

Fourier transform infrared (FT-IR) spectroscopy analysis

Figure 3 shows the Fourier-transform infrared (FT-IR) spectra of Fe-MCM-41 with varying iron loadings (x Fe^{3+}: SiO_2, where x = 0.04, 0.08, 0.12, and 0.16). All Fe-MCM-41 samples exhibit a broad absorption band in the range of 3600–3000 cm^{-1}, attributed to the characteristic absorption of silanol (Si–OH) groups on the surface of the mesoporous material. An absorption peak around 1640 cm^{-1} is observed, attributed to the vibrational absorption of O–H bonds, indicating a small amount of adsorbed water in the samples. Two distinct absorption peaks are observed at 820 cm^{-1} and 480 cm^{-1} in the infrared spectra. The peak at 820 cm^{-1} corresponds to the symmetric stretching vibration of Si–O bonds in the silicate tetrahedral structure, while the peak at 480 cm^{-1} corresponds to the bending vibration of Si–O bonds. These absorption peaks are consistent with findings

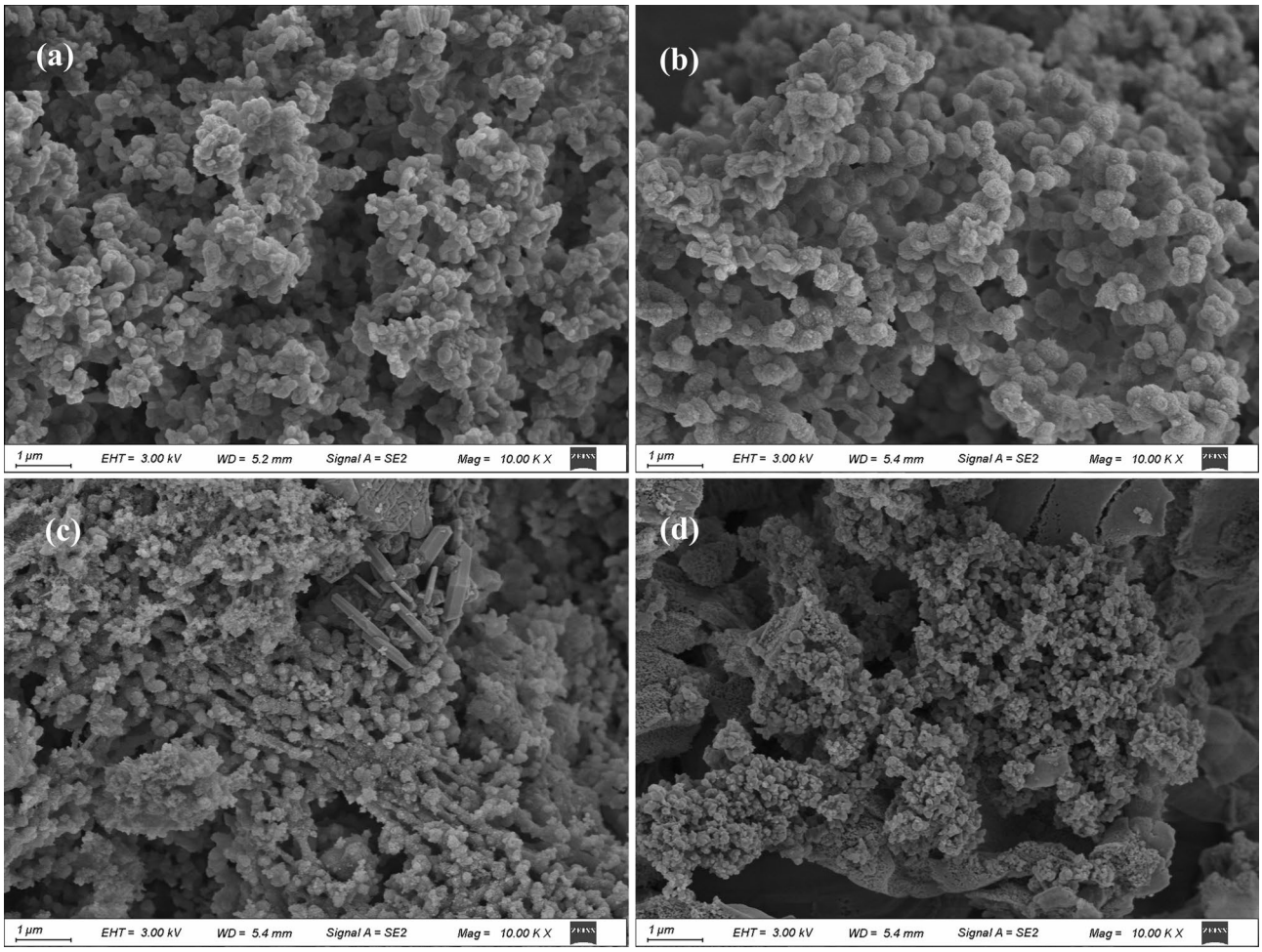

Fig. 2. SEM images of Fe-MCM-41 with varying Iron Contents. (**a**) x = 0.04; (**b**) x = 0.08; (**c**) x = 0.12; (**d**) x = 0.16.

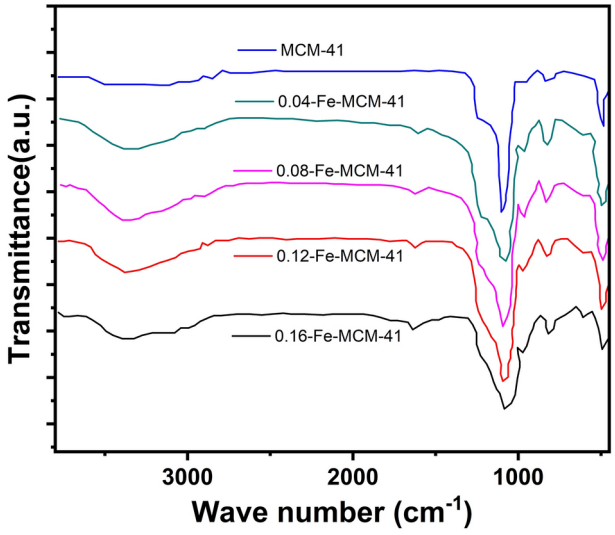

Fig. 3. FT-IR spectra of Fe-MCM-41 with varying Iron Contents.

Sample	xFe^{3+} : SiO_2	Iron content (theoretical value) (wt%)	Iron content (actual value by XRF measurement method) (wt%)
0.04-Fe-MCM-41	0.04	3.60	3.38
0.08-Fe-MCM-41	0.08	6.94	5.67
0.12-Fe-MCM-41	0.12	10.07	9.69
0.16-Fe-MCM-41	0.16	13.00	12.66

Table 3. Iron content in Fe-MCM-41 with varying Fe^{3+} ratios.

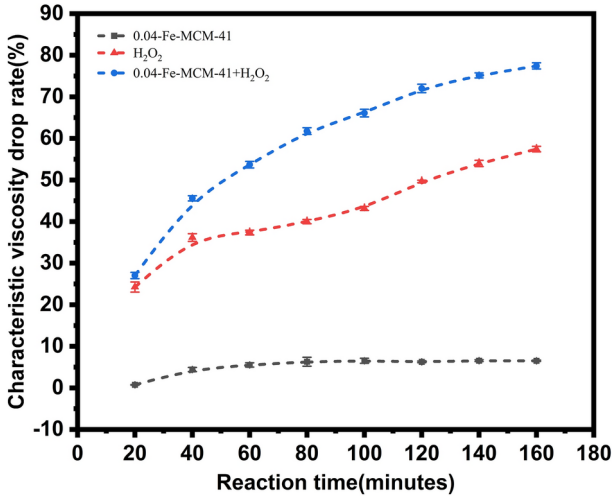

Fig. 4. Effects of different degradation systems on chitosan degradation efficiency.

reported in the literature[33,34], confirming the structural integrity of the silicate tetrahedra in the Fe-MCM-41 materials.

The figure shows that, compared to pure silica MCM-41, the absorption peak intensity at 963 cm^{-1} in the Fe-doped Fe-MCM-41 samples is significantly enhanced. This enhancement serves as indirect evidence of successful iron incorporation into the framework. Additionally, the absorption peak around 1080 cm^{-1} is attributed to the asymmetric stretching vibrations of Si–O–Si bonds in the silicate tetrahedra. In pure silica MCM-41, this peak typically appears at 1100 cm^{-1}. In contrast, the strong absorption peak at 1080 cm^{-1} in the Fe-MCM-41 samples indicates a shift of the Si–O–Si peak to lower wave numbers. This shift further confirms that iron has been incorporated into the MCM-41 framework, causing subtle structural changes. The shift in the Si–O–Si absorption peak signifies not only successful iron doping but also microstructural alterations in the framework.

Iron content (XRF) analysis

Table 3 shows the iron content of Fe-MCM-41 with varying molar ratios (x Fe^{3+}: SiO_2, where x = 0.04, 0.08, 0.12, and 0.16). As the molar ratio of iron ions to SiO_2 increases, the iron content in Fe-MCM-41 also increases. The XRF-measured values for the four Fe-MCM-41 samples are slightly lower than their theoretical values, suggesting that most of the iron ions were successfully incorporated into the mesoporous molecular sieve.

Evaluation of catalyst activity

Screening of degradation systems

The effects of different degradation systems on chitosan degradation under identical conditions were studied. The degradation systems included the Fe-MCM-41 system (0.5 g/L of 0.04-Fe-MCM-41 catalyst), the H_2O_2 system (0.86 mol/L H_2O_2), and the Fe-MCM-41 Fenton-like system (0.5 g/L of 0.04-Fe-MCM-41 catalyst combined with 0.86 mol/L H_2O_2). In all experiments, the chitosan concentration was kept at 5 g/L, the CH_3COOH concentration at 0.32 mol/L, and the reaction temperature at 30 °C. The reaction time ranged from 20 to 160 min. The experimental results in Fig. 4 illustrate the effects of different degradation systems on chitosan degradation.

Figure 4 shows the influence of various degradation systems on chitosan degradation, further confirming the superior performance of Fe-MCM-41 in Fenton-like catalytic reactions. Under identical conditions, after 160 min, the Fe-MCM-41 system showed a viscosity reduction rate of only 6.4%, indicating that the degradation was primarily driven by acid-catalyzed depolymerization. However, with the addition of H_2O_2, the viscosity reduction rate increased significantly to 56%, demonstrating that H_2O_2 substantially enhanced the degradation of chitosan. This enhancement is attributed to the generation of small quantities of radicals (e.g., $^{\cdot}OH$) by H_2O_2, which attack chitosan molecular chains.

With the introduction of Fe-MCM-41 into the H_2O_2 system, forming a highly efficient Fenton-like multiphase catalytic system, the viscosity reduction rate increased further to 77.4%. This significant enhancement suggests

that Fe-MCM-41 not only effectively catalyzed the decomposition of H_2O_2 to generate more ·OH radicals, but also that these radicals played a key role in the cleavage of chitosan molecular chains. The improved degradation efficiency is mainly attributed to the porous structure of Fe-MCM-41 and the uniform distribution of iron ions, enabling more efficient capture and activation of H_2O_2. The iron ions within and on the surface of Fe-MCM-41 pores react with H_2O_2, forming a Fenton-like system that significantly enhances ·OH radical production. As a highly oxidative radical, ·OH effectively attacks the glycosidic bonds of chitosan, accelerating its decomposition[35].

Furthermore, the unique porous structure of Fe-MCM-41 imparts superior multiphase catalytic properties in Fenton reactions. This structure provides abundant active sites, improving contact efficiency between reactants and the catalyst, thereby accelerating the reaction rate and enhancing product yield. Compared to homogeneous Fenton systems, Fe-MCM-41 catalysts exhibit excellent recyclability and stability, preventing iron ion leaching, extending the catalyst's lifespan, and reducing environmental pollution risks.

The effect of varying iron loadings in Fe-MCM-41 on chitosan degradation efficiency

The effect of varying iron loadings in Fe-MCM-41 (1.0 SiO_2: x Fe^{3+}, where x denotes the molar ratio of $Fe(NO_3)_3{\cdot}9H_2O$, ranging from 0.04 to 0.16) on chitosan degradation was investigated. Under conditions of 5 g/L chitosan, 0.5 g/L Fe-MCM-41 catalyst, 0.86 mol/L H_2O_2, 0.32 mol/L CH_3COOH, and 30 °C, the reaction time ranged from 20 to 160 min. The experimental results in Fig. 5 demonstrate the influence of iron loading on the efficiency of chitosan degradation.

Figure 5 shows that iron loading in Fe-MCM-41 significantly impacts chitosan degradation efficiency. Under identical conditions, Fe-MCM-41 samples with varying iron contents all exhibited good catalytic performance, primarily due to the introduction of iron, which increases the number of Lewis acid sites on the catalyst surface. This promotes the decomposition of H_2O_2, generating more hydroxyl radicals (·OH), which accelerate chitosan degradation[36]. Appropriate iron loading helps maintain the mesoporous structure and large specific surface area of Fe-MCM-41, which is crucial for improving catalytic efficiency.

The balance of iron loading is a critical factor influencing catalytic activity. Moderate iron incorporation can significantly increase the number of active sites (acid sites) on Fe-MCM-41, thereby enhancing its catalytic activity. However, excessive iron loading may cause partial pore blockage, reducing specific surface area and limiting the effective contact between reactants and H_2O_2 on the catalyst surface, thus diminishing catalytic performance[37]. Experimental results show that when the iron content reaches x = 0.12, the catalytic performance of Fe-MCM-41 reaches its optimal level. Under these conditions, an ideal balance is achieved between the number of acid sites and the specific surface area (665.71 m^2/g), providing sufficient active sites while preserving an effective pore structure, ensuring the synergistic effects of H_2O_2 decomposition and chitosan adsorption[38]. After 140 min of reaction, the viscosity reduction rate of chitosan reached 82.2%, a 28.1% improvement in degradation efficiency compared to the system using only H_2O_2.

The 0.12-Fe-MCM-41 catalyst maintains a large specific surface area, even with higher iron content, and demonstrates superior efficiency in chitosan degradation. This suggests that the optimized Fe-MCM-41 catalyst achieves an optimal balance between iron loading and performance, demonstrating greater practical utility. However, when the iron content increases to x = 0.16, despite the continued rise in the number of acid sites, excessive iron introduction leads to a sharp decline in specific surface area to 350.28 m^2/g, damaging the pore structure. This restricts the diffusion and contact of reactants, reducing chitosan degradation efficiency to 73.1%. These results show that while higher iron loading increases the number of acid sites, the damage to the pore structure and the reduction in specific surface area significantly weaken overall catalytic activity[39].

Therefore, Fe-MCM-41 with an iron content of x = 0.12 achieves optimal catalytic degradation through moderate iron loading, a well-balanced distribution of acid sites, and a relatively large specific surface area, suggesting that the optimal reaction time is 140 min.

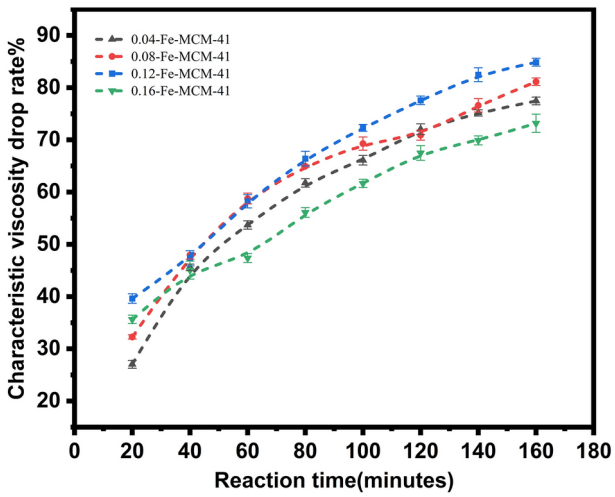

Fig. 5. Effects of iron loading in Fe-MCM-41 on chitosan degradation efficiency.

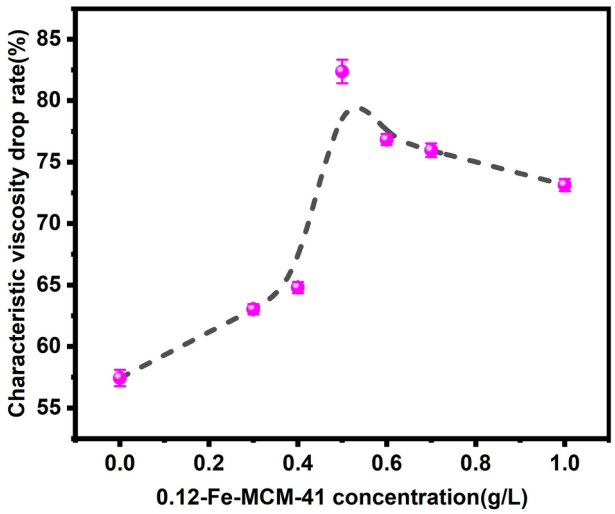

Fig. 6. Effects of Fe-MCM-41 concentration on chitosan degradation efficiency.

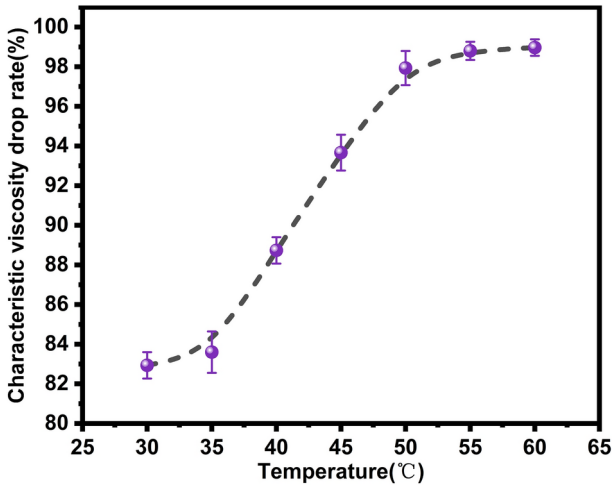

Fig. 7. Effects of reaction temperature on chitosan degradation efficiency.

The effect of Fe-MCM-41 concentration on chitosan degradation efficiency

The effect of varying 0.12-Fe-MCM-41 concentrations (0–1 g/L) on chitosan degradation efficiency was investigated. The experimental conditions included 5 g/L chitosan, 0.86 mol/L H_2O_2, 0.32 mol/L CH_3COOH, a reaction temperature of 30 °C, and a reaction time of 140 min. The experimental results in Fig. 6 show the effect of varying 0.12-Fe-MCM-41 concentrations on chitosan degradation efficiency.

As shown in Fig. 6, Fe-MCM-41 concentration significantly influences chitosan degradation efficiency. Under identical conditions, the viscosity reduction rate of chitosan increases with the Fe-MCM-41 catalyst concentration. At a catalyst concentration of 0.5 g/L, the viscosity reduction rate of chitosan reaches 82.2%, indicating optimal catalytic efficiency. However, increasing the catalyst concentration beyond 0.5 g/L decreases the viscosity reduction rate. Further increases in catalyst concentration continue to reduce the viscosity reduction rate. This observation aligns with findings reported in reference[40], and confirms that excessively high catalyst concentrations may induce an anti-catalytic effect. Therefore, under the given conditions, the optimal catalyst concentration is 0.5 g/L.

The effect of reaction temperature on chitosan degradation efficiency

The effect of varying reaction temperatures (30–60 °C) on chitosan degradation efficiency was investigated. The experimental conditions included 5 g/L chitosan, 0.5 g/L 0.12-Fe-MCM-41, 0.86 mol/L H_2O_2, 0.32 mol/L CH_3COOH, and a reaction time of 140 min. The experimental results in Fig. 7 show the influence of varying reaction temperatures on chitosan degradation efficiency.

As shown in Fig. 7, reaction temperature significantly influences chitosan degradation efficiency. At 30 °C, the viscosity reduction rate of chitosan reaches 82.2% under the same reaction conditions. As the reaction temperature increases, the viscosity reduction rate of chitosan rises accordingly. At 50 °C, the viscosity

reduction rate reaches 98.2%, reflecting a 16% increase compared to 30 °C. This increase is attributed to the higher number of activated molecules within a certain temperature range, enhancing the probability of effective collisions and facilitating the cleavage of glycosidic bonds in chitosan molecules[41]. When the temperature exceeds 50 °C, the viscosity reduction rate plateaus. This may be due to excessively high temperatures causing partial decomposition of H_2O_2, hindering hydroxyl radical formation[42]. Additionally, excessively high reaction temperatures hinder hydroxyl radical adsorption on Fe-MCM-41, negatively impacting the Fenton-like reaction and reducing degradation efficiency. Therefore, under these conditions, the optimal reaction temperature for chitosan degradation is 50 °C.

The effect of CH_3COOH concentration on chitosan degradation efficiency

The effect of varying CH_3COOH concentrations (0–0.32 mol/L) on chitosan degradation efficiency was investigated. The experimental conditions included 5 g/L chitosan, 0.5 g/L 0.12-Fe-MCM-41, 0.86 mol/L H_2O_2, a reaction temperature of 50 °C, and a reaction time of 140 min. The results in Fig. 8 show the effect of varying acetic acid (CH_3COOH) concentrations on chitosan degradation efficiency.

As shown in Fig. 8, CH_3COOH concentration significantly influences chitosan degradation efficiency. Under identical conditions, at a CH_3COOH concentration of 0.016 mol/L, the viscosity reduction rate of chitosan is 88.9%. As the CH_3COOH concentration increases, the viscosity reduction rate rises to 98.2% at 0.16 mol/L. These results suggest that within a certain concentration range, increasing CH_3COOH concentration significantly enhances chitosan degradation efficiency.

First, CH_3COOH (acetic acid), as an acidic medium, provides sufficient H^+ ions in the reaction system, enhancing the activity of the Fe-MCM-41 catalyst. The acidic environment facilitates H_2O_2 decomposition, generating more hydroxyl radicals ($^{\cdot}OH$), which accelerates the cleavage of glycosidic bonds in chitosan molecules. As CH_3COOH concentration increases, the H^+ concentration in the reaction system rises, enhancing the acidity of active sites on the catalyst and making chitosan molecules more susceptible to $^{\cdot}OH$ attack, thereby significantly improving degradation efficiency[43].

However, when CH_3COOH concentration exceeds 0.16 mol/L, the viscosity reduction rate stabilizes. This may be due to several factors. First, an excessively high concentration of H^+ may bind to the amine groups ($-NH_2$) in chitosan, forming a cationic system ($R\text{-}NH_3^+$), limiting the attack sites for hydroxyl radicals and slowing degradation. Additionally, a highly acidic environment may accelerate H_2O_2 decomposition, leading to excessive consumption before sufficient reaction occurs, reducing $^{\cdot}OH$ generation and ultimately limiting degradation efficiency[20].

Therefore, under these conditions, the optimal CH_3COOH concentration is 0.16 mol/L. At this concentration, H^+ in the reaction system effectively promotes hydroxyl radical generation and chitosan degradation, without inhibiting $^{\cdot}OH$ action sites or causing excessive H_2O_2 consumption, thus maximizing degradation efficiency.

The effect of H_2O_2 concentration on chitosan degradation efficiency

The effect of varying H_2O_2 concentrations (0–1 mol/L) on chitosan degradation efficiency was investigated. The experimental conditions included 5 g/L chitosan, 0.5 g/L 0.12-Fe-MCM-41, 0.16 mol/L CH_3COOH, a reaction temperature of 50 °C, and a reaction time of 140 min. The results in Fig. 9 show the effect of varying H_2O_2 concentrations on chitosan degradation efficiency.

As demonstrated in Fig. 9, the concentration of H_2O_2 has a significant impact on chitosan degradation efficiency. Under identical reaction conditions, when no H_2O_2 is present, only acid-mediated degradation occurs, resulting in a viscosity reduction of 6.4%. This result indicates that without H_2O_2, degradation is primarily driven by the acidic medium and is limited in effectiveness. As the H_2O_2 concentration increases, chitosan degradation efficiency is significantly enhanced. At 0.86 mol/L H_2O_2, the viscosity reduction rate of chitosan reaches 98.2%. This is because H_2O_2 is the primary source of $^{\cdot}OH$, and its concentration directly affects the

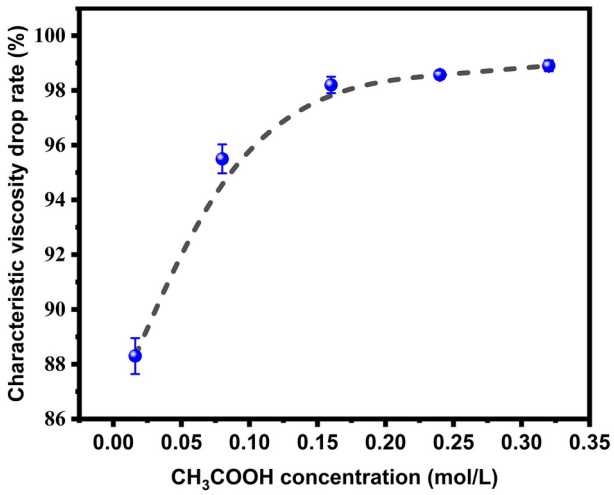

Fig. 8. Effects of CH_3COOH concentration on chitosan degradation efficiency.

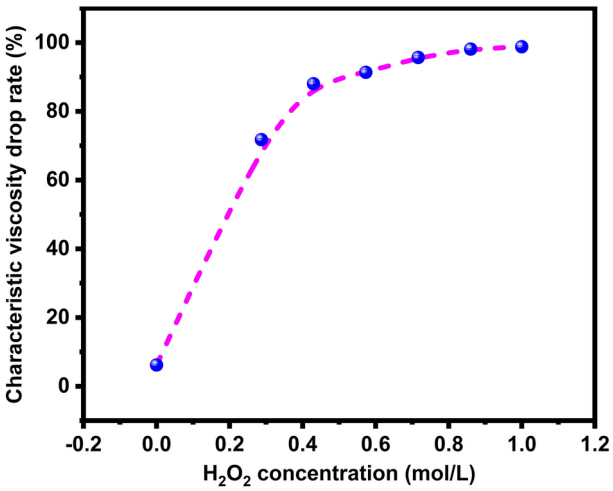

Fig. 9. Effects of H_2O_2 concentration on chitosan degradation efficiency.

amount of hydroxyl radicals produced, which are essential for degradation efficiency[44]. In Fenton-like systems, H_2O_2 decomposes under Fe-MCM-41 catalysis, generating ·OH radicals that attack glycosidic bonds in chitosan molecules, cleaving them into smaller fragments. Thus, increasing H_2O_2 concentration significantly enhances ·OH generation, accelerating chitosan degradation.

Within a certain range, increasing H_2O_2 concentration improves chitosan degradation efficiency. However, when H_2O_2 concentration exceeds 0.86 mol/L, the viscosity reduction rate plateaus. Several factors contribute to this phenomenon. Excessive H_2O_2 may promote ·OH generation but also react with ·OH, producing water (H_2O) and oxygen (O_2). These side reactions consume ·OH, reducing the number of active species available to attack chitosan and limiting further improvements in degradation efficiency. As chitosan degrades into smaller, more soluble molecules, the number of free amine groups available for ·OH attack decreases, making further oxidative cleavage of acetyl groups more difficult[45]. This explains why degradation efficiency plateaus at high H_2O_2 concentrations.

In addition, too high a concentration of H_2O_2 may cause incomplete decomposing of the H_2O_2 in the system. The remaining H_2O_2 may impose an inhibitory effect on other reactants or products in the solution, interfering with the normal Fenton-like reaction process. Meanwhile, oxygen bubbles formed during the reaction may cover the surface of the catalyst, reducing the contact opportunities between the reactants and the catalyst, further reducing the reaction efficiency. Therefore, under the conditions of this study, the optimal concentration of H_2O_2 is 0.86 mol/L. This concentration maximizes the production of ·OH while avoiding side reactions caused by excess H_2O_2 and its potential negative impact on catalyst activity. By optimizing the H_2O_2 concentration, this study significantly improved the degradation efficiency of chitosan and achieved the best results.

The effect of chitosan concentration on degradation efficiency

The effect of varying chitosan concentrations (2–15 g/L) on degradation efficiency was studied. The experimental conditions included 0.5 g/L 0.12-Fe-MCM-41, 0.16 mol/L CH_3COOH, 0.86 mol/L H_2O_2, a reaction temperature of 50 °C, and a reaction time of 140 min. The results in Fig. 10 show the effect of varying chitosan concentrations on degradation efficiency.

As shown in Fig. 10, the mass concentration of chitosan has a significant impact on its degradation effect. Under the same reaction conditions, when the chitosan mass concentration is 2 g/L, the intrinsic viscosity decrease rate reaches 99.3%. However, as the concentration of chitosan increases, when its concentration increases to 15 g/L, the intrinsic viscosity decrease rate is only 90.3%, indicating that its degradation efficiency decreases as the concentration increases. This phenomenon is mainly due to the fact that when the mass concentration of chitosan is low, the number of molecular chains is smaller and the entanglement between molecular chains is reduced. This results in reduced hydrogen bonding within and between molecules, which in turn increases the possibility of hydroxyl radicals attacking the 1,4-glycosidic bonds in chitosan[22]. Therefore, within the concentration range of the experiment, lower mass concentration of chitosan favors the oxidative degradation.

The reusability of Fe-MCM-41

The reusability of 0.12-Fe-MCM-41 was studied under conditions of 5 g/L chitosan, 0.5 g/L 0.12-Fe-MCM-41, 0.16 mol/L CH_3COOH, 0.86 mol/L H_2O_2, a reaction temperature of 50 °C, and a reaction time of 140 min. After filtration, washing with deionized water, and drying, the used catalyst was recovered for reuse. The iron content of the recovered catalyst was measured using XRF after each reuse cycle. Table 4 illustrate the viscosity reduction of chitosan over the number of catalyst reuse cycles.

As shown in Table 4, the 0.12-Fe-MCM-41 catalyst maintained a viscosity reduction rate above 93.6% over the first four cycles, demonstrating high reusability. However, in the fifth cycle, the catalytic degradation activity decreased significantly, and the intrinsic viscosity decrease rate dropped to 85.8%. In order to explore the reasons

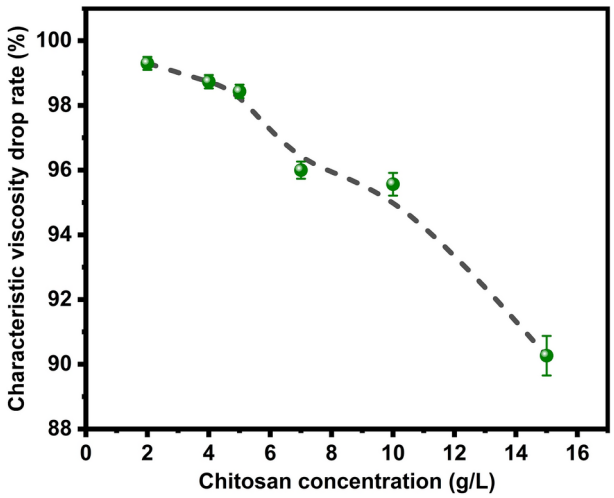

Fig. 10. Effects of chitosan concentration on its degradation efficiency.

No. of recycling	The characteristic viscosity decrease rate (%)
1	98.2
2	97.7
3	96.8
4	93.6
5	85.8

Table 4. Reusability of 0.12-Fe-MCM-41 catalyst.

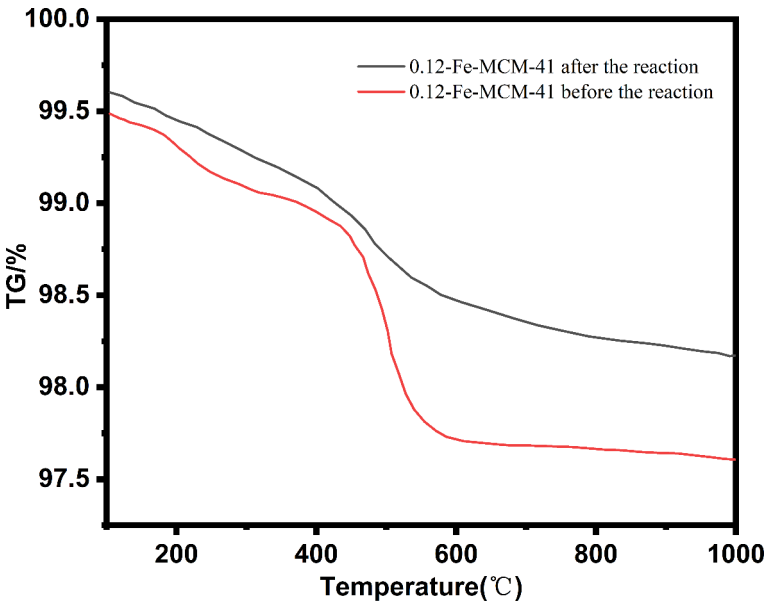

Fig. 11. Thermogravimetric analysis (TGA) graphs of 0.12-Fe-MCM-41 before and after treatment.

for the change in activity of the 0.12-Fe-MCM-41 catalyst after recycling, thermogravimetric analysis (TGA) was used to compare the unused catalyst and the catalyst samples after five cycles. The analysis results show that there are significant differences in the mass loss of the two samples at different temperature intervals.

As demonstrated in Fig. 11, in the low-temperature range (100–200 °C), the mass loss of the unused catalyst was relatively small, primarily due to the desorption of adsorbed water. By contrast, the reused catalyst exhibited

significantly higher mass loss, indicating an accumulation of reaction products or adsorbed moisture within the pores.

In the medium temperature range of 200–500 °C, the mass loss of the unused catalyst is still small, while the mass loss of the recycled catalyst increases significantly, showing that organic matter or carbon deposits are deposited in the pores, covering the active sites and hindering. The contact of reactants is reduced, resulting in a decrease in catalyst activity[46]. In the high-temperature range (above 500 °C), the mass change of the unused catalyst was minimal, indicating its structural stability. However, the reused catalyst exhibited considerable mass loss, indicating partial degradation of its silica–carbon framework after multiple cycles.

In summary, the decline in 0.12-Fe-MCM-41 catalyst activity after several recycles is primarily caused by the accumulation of organic materials and carbon deposits, which lead to pore blockage and active site coverage, as well as partial framework collapse. These factors collectively affected the stability and catalytic performance of the catalyst[47].

The stability of Fe-MCM-41 catalyst in the catalysis of H_2O_2

The iron dissolution of the 0.12-Fe-MCM-41 catalyst was analyzed using Inductively Coupled Plasma Optical Emission Spectroscopy (ICP-OES), with X-Ray Fluorescence (XRF) determining the iron content to be 9.69 wt%. Under the described reaction conditions, the Fe leaching rate was 0.48 mg/L. With a catalyst dosage of 0.5 g/L, the calculated iron leaching rate was 0.99%. The lower dissolution amount indicates that the catalyst has good stability and effectively avoids the secondary pollution problem caused by the dissolution of a large amount of metal ions from the framework.

However, it should be noted that this part of dissolved iron may mainly come from the surface of the catalyst rather than the iron atoms deep in the framework structure. The leaching of surface iron may result from the partial dissolution of exposed Fe^{3+} or Fe^{2+} ions during contact with the reaction solution. This phenomenon is especially relevant for Fe-MCM-41 catalysts synthesized via hydrothermal methods, which may lead to partial surface distribution of iron. The weakening and leaching of surface iron ions may be unavoidable[15,26].

Nevertheless, the catalyst recovery in this experiment did not involve high-temperature calcination or complex regeneration procedures. The Fe-MCM-41 catalyst exhibited an acceptable leaching rate, demonstrating good stability after multiple uses. Despite minor surface iron leaching, the reusability of Fe-MCM-41 in industrial applications remains satisfactory. The low iron leaching rate suggests that the catalyst can maintain structural integrity and catalytic activity. No significant increase of metal ion concentration in the solution. This mitigates the risk of secondary pollution.

In summary, Fe-MCM-41 exhibits good stability and durability, making it suitable for recycling in practical production processes and highlighting its significant application potential.

Study on the kinetics of catalytic degradation

Apparent rate constants of chitosan degradation at different reaction temperatures

To investigate the kinetic characteristics of Fe-MCM-41 in chitosan degradation, experiments were conducted under the following conditions: 5 g/L chitosan, 0.5 g/L 0.12-Fe-MCM-41, 0.16 mol/L CH_3COOH, 0.86 mol/L H_2O_2, and a reaction time of 140 min. The experiments were conducted at 313 K and 323 K, respectively. The catalytic degradation rate of chitosan can be expressed as $-\frac{dc}{dt} = kc^n$, where "c" represents chitosan concentration, "k" is the rate constant, "n" is the reaction order, and "t" is time. Graphs were plotted from the experimental results (see Fig. 12) to examine the relationship between the first-order reaction $-\ln(1-\eta r)$ and reaction time, as well as the second-order reaction $1/(1-\eta r)$ and reaction time.

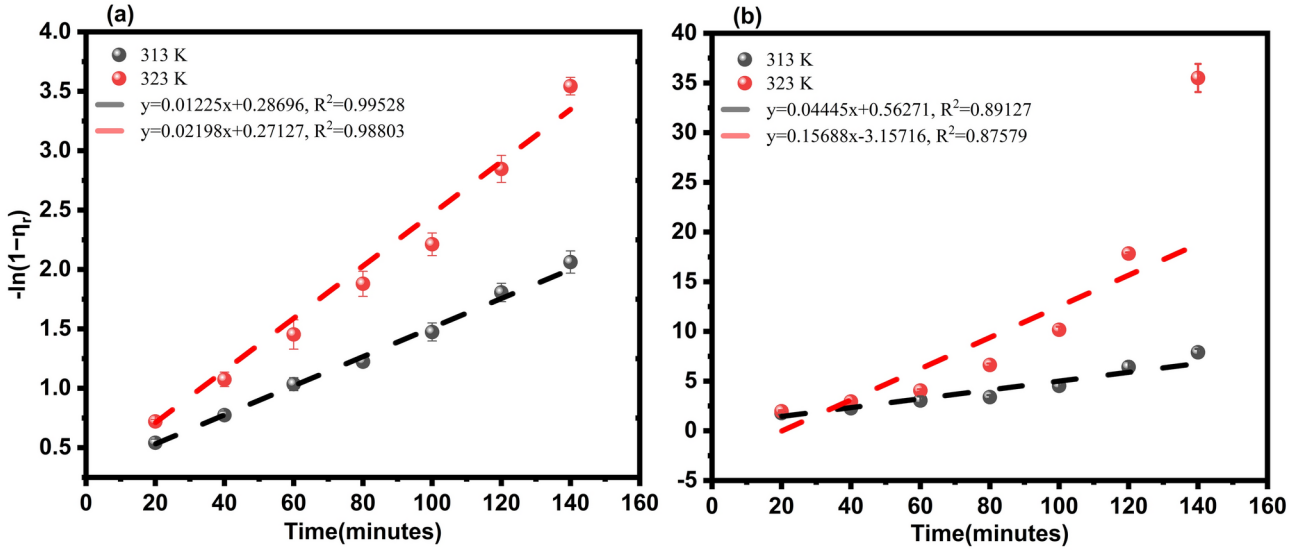

Fig. 12. Kinetic curves of chitosan degradation. (**a**) First-order reaction; (**b**) Second-order reaction.

T (K)	First-order rate constant k_1 (min^{-1})	First-order R^2	Second-order rate constant k_2 (min^{-1})	Second-order R^2
313	0.01225	0.99528	0.04445	0.89127
323	0.02198	0.98803	0.15688	0.87579

Table 5. Apparent rate constants for chitosan degradation at various temperatures.

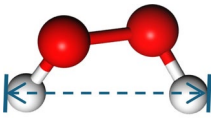

Fig. 13. Maximum Diameter of H_2O_2.

A comparison of Fig. 12 and Table 5 reveals that the first-order kinetic model ($R^2 > 0.95$) shows a better correlation than the second-order kinetic model ($R^2 < 0.95$) at both temperatures. Therefore, it can be inferred that the oxidative degradation of chitosan in the Fe-MCM-41 heterogeneous Fenton-like system follows first-order kinetics.

Apparent kinetic equation for chitosan degradation

According to the Arrhenius equation, the rate constants for reaction at two temperatures ($T_2 = 313$ K and $T_1 = 323$ K) were used for integration: $\ln\frac{k(T_2)}{k(T_1)} = \frac{E_a(T_2-T_1)}{RT_2T_1}$, where "$R$" is the molar gas constant. By substituting the rate constants into the Arrhenius equation, the apparent activation energy (Ea) was determined to be 48.91 kJ/mol, and the pre-exponential factor was calculated as 1.38×10^8 min^{-1}. Thus, the apparent kinetic equation for chitosan degradation can be expressed as: $k = 1.38 \times 10^8 \exp\left(-4.891 \times 10^4/\mathrm{RT}\right)$.

Reaction mechanism in the catalysis of H_2O_2 by Fe-MCM-41

Comparison of pore size of Fe-MCM-41 and molecular size of H_2O_2

BET analysis revealed that the average mesopore diameters of 0.04-Fe-MCM-41, 0.08-Fe-MCM-41, 0.12-Fe-MCM-41, and 0.16-Fe-MCM-41 were 3.61 nm, 3.54 nm, 3.06 nm, and 2.67 nm, respectively which was in consistent with literature value (approx 3 nm)[48]. Metal doping reduces both the pore volume and pore diameter of MCM-41 mesoporous molecular sieves[49]. Under ideal conditions, without considering hydration effects, the longest dimension of H_2O_2 is 0.48 nm (see Fig. 13), while the average pore diameter of the four Fe-MCM-41 samples is 3.22 nm. Therefore, H_2O_2 can smoothly pass through the molecular sieve channels, and its catalytic performance is minimally influenced by spatial hindrance.

Analysis of the zero-point charge of Fe-MCM-41

Figure 14 shows the zeta potential of 0.12-Fe-MCM-41 under different pH conditions, with the point of zero charge (PZC) occurring at pH 2. Under mildly acidic conditions ($2 < pH < 7$), the mesoporous material surface carries a negative charge, while H_2O_2 molecules remain neutral. Therefore, in mildly acidic environments, the negative charge on the surface of 0.12-Fe-MCM-41 neither repels nor attracts H_2O_2 molecules significantly, minimizing the influence of surface charge on H_2O_2 interactions.

Reaction process of H_2O_2 catalyzed by Fe-MCM-41

Based on the above analysis, steric hindrance and electrostatic effects on H_2O_2 molecules in the Fe-MCM-41 catalyst are relatively weak. As shown in Fig. 15, after H_2O_2 passes through the internal channels of Fe-MCM-41 smoothly, it undergoes a Fenton-like reaction with $\equiv Fe^{III}$ on the catalyst surface and within the channels, producing $\equiv Fe^{II}$ and $HO_2^{\cdot}$ (Eq. 1). Subsequently, $\equiv Fe^{II}$ further reacts with H_2O_2 in a Fenton reaction, generating $\equiv Fe^{III}$ and $^{\cdot}OH$ (Eq. 2). The cyclic transformation between $\equiv Fe^{II}$ and $\equiv Fe^{III}$ on the catalyst promotes continuous H_2O_2 decomposition to generate $^{\cdot}OH$, thereby facilitating chitosan degradation. The degradation rate of chitosan and the consumption of H_2O_2 both indicate that Fe-MCM-41 plays a crucial role in catalyzing the decomposition of H_2O_2 to generate $^{\cdot}OH$. By characterizing the structure and surface properties of Fe-MCM-41, it was found that the catalyst has a high specific surface area and uniformly distributed iron active sites, which allows H_2O_2 to diffuse effectively and contact these active sites, promoting the Fenton-like reaction[50]. These experimental data, combined with mechanistic analysis, clearly illustrate the key role of Fe-MCM-41 in the decomposition of H_2O_2 and the generation of $^{\cdot}OH$, providing solid theoretical support for its potential in practical applications.

$$\equiv Fe^{III} + H_2O_2 \rightarrow \equiv Fe^{II} + HO_2^{\cdot} + H^+ \quad (1)$$

$$\equiv Fe^{II} + H_2O_2 \rightarrow \equiv Fe^{III} + {}^{\cdot}OH + OH^- \quad (2)$$

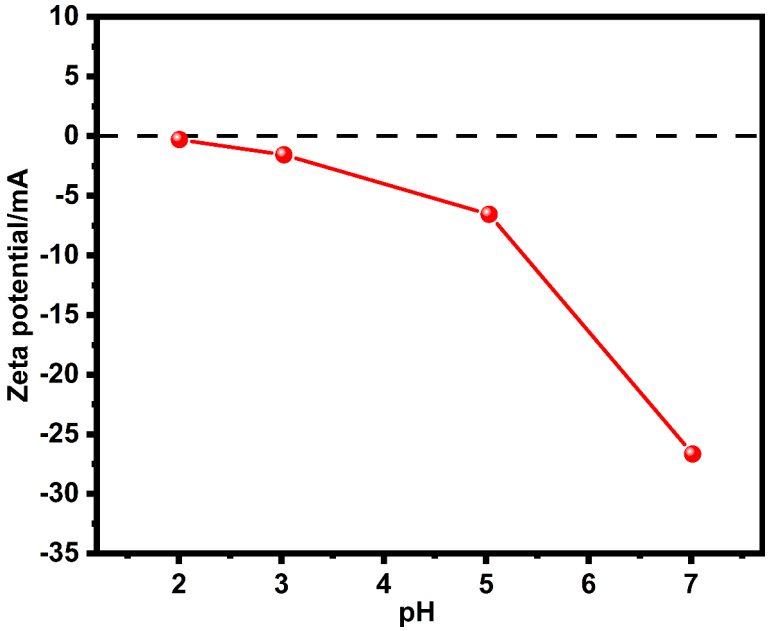

Fig. 14. Zeta Potential Graph of 0.12-Fe-MCM-41.

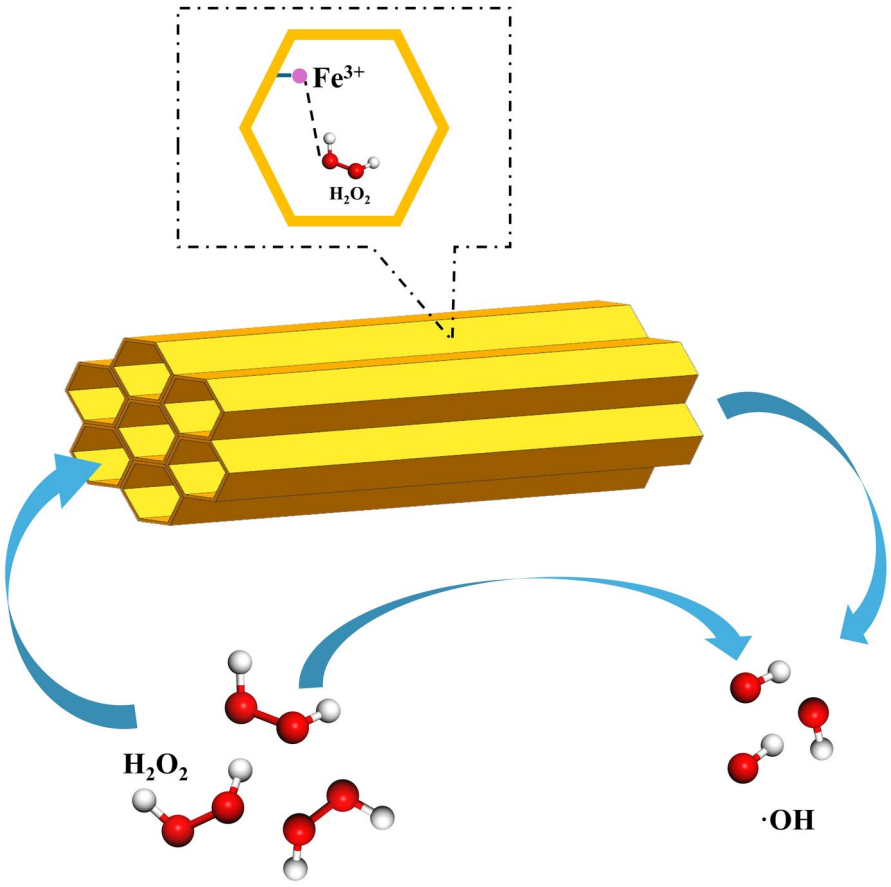

Fig. 15. Reaction Process of Fe-MCM-41 Catalyzing H_2O_2

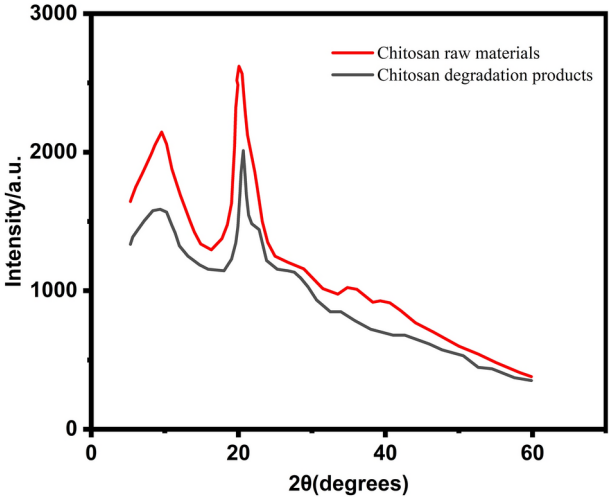

Fig. 16. XRD Patterns of Chitosan Raw Material and Chitosan Degradation Products.

XRD analysis of chitosan degradation products

As shown in Fig. 16, raw chitosan exhibits two characteristic diffraction peaks at 2θ = 9.55° and 20.07°, while the degradation products show peaks at 2θ = 9.36° and 20.65°. Compared to raw chitosan, the characteristic peaks of the degraded chitosan were weakened, but their positions remain largely unchanged. This indicates that, under the catalytic influence of Fe-MCM-41, chitosan undergoes oxidative degradation without significant change of its fundamental functional groups and main chain structure[22]. This suggests that degradation primarily affects the glycosidic bonds of chitosan, rather than causing substantial changes to its main chain or functional groups.

During the catalytic oxidative degradation process, as hydroxyl radicals (·OH) are generated and participate in the reaction, the glycosidic bonds of chitosan are gradually broken, resulting in a shortening of the molecular chain length, weakening of the intermolecular hydrogen bonding effect, and loosening of the molecular chain arrangement, which ultimately leads to a decrease in the crystallinity of chitosan[51].

Conclusion

(1) This study establishes a Fenton-like heterogeneous catalytic system utilizing Fe-MCM-41 for the efficient oxidative degradation of chitosan. This system effectively addresses the challenges posed by traditional homogeneous Fenton systems, including difficulties in catalyst recovery and secondary pollution from residual iron ions, while significantly enhances degradation efficiency. Experimental results indicate that the degradation efficiency of the Fe-MCM-41 system is 28.1% higher than that of the system using only H_2O_2, highlighting its superior activation capability for H_2O_2. Under optimized conditions (Fe-MCM-41 concentration of 0.5 g/L, chitosan concentration of 5 g/L, CH_3COOH concentration of 0.16 mol/L, H_2O_2 concentration of 0.86 mol/L, temperature of 50°C, and reaction time of 140 minutes), the intrinsic viscosity reduction rate of chitosan reached 98.2%.

(2) The iron loading in the Fe-MCM-41 catalyst significantly affects the degradation performance. The optimal performance occurred with x = 0.12, whereby the degradation efficiency retained >93.6% after four recycles, which demonstrated excellent stability and reusability for industrial applications.

(3) Kinetic analysis concluded that the degradation of chitosan follows a first-order reaction kinetic model, with an apparent activation energy of 48.91 kJ/mol. Based on Arrhenius equation, the calculated kinetic equation is $k = 1.38 \times 10^8 \exp(-4.891 \times 10^4 / RT)$, indicating that the reaction rate significantly increases with rising temperature.

(4) This study represents a significant progress in applying the Fe-MCM-41 catalyst, offering an effective solution for the efficient degradation of chitosan. The system not only enhances degradation efficiency but also demonstrates good recoverability and stability, providing technical support for the further application of chitosan in various biomaterials and related fields. Future research will focus on the optimization of the catalytic activity and stability of Fe-MCM-41 through metal ion doping, evaluation of broader application potential in treating chitosan and other related polysaccharide materials.

Data availability

The authors confirm that the data supporting the findings of this study are available within the article.

Received: 23 August 2024; Accepted: 14 October 2024
Published online: 29 October 2024

References

1. Khubiev, O. M. et al. Chitosan-based antibacterial films for biomedical and food applications. *Int. J. Mol. Sci.* **24**(13), 10738 (2023).

2. Zhang, M. et al. Application of Chitosan and its derivative polymers in clinical medicine and agriculture. *Polymers* **14**(5), 958 (2022).
3. Benchamas, G. et al. Preparation and biological activities of chitosan oligosaccharides. *Trends Food Sci. Technol.* **107**, 38–44 (2021).
4. Jafari, H. et al. Development of marine oligosaccharides for potential wound healing biomaterials engineering. *Chem. Eng. J. Adv.* **15**, 100113 (2021).
5. Gonçalves, C., Ferreira, N. & Lourenço, L. Production of low molecular weight Chitosan and chitooligosaccharides (COS): A review. *Polymers* **13**(15), 2466 (2021).
6. Ding, X. et al. Hydroxyl and sulfate radical-based oxidation of RhB dye in UV/H_2O_2 and UV/persulfate systems: Kinetics, mechanisms, and comparison. *Chemosphere* **253**, 126655 (2020).
7. Chen, Y. et al. Influence of molecular weight of polysaccharides from Laminaria japonica to LJP-based hydrogels: Anti-inflammatory activity in the wound healing process. *Molecules* **27**(1), 6915 (2022).
8. Chu, Y. et al. Enhanced electro-reduction of Fe^{3+} to Fe^{2+} by acidified carbon nanotube-modified graphite cathode and its application in a novel Fenton process for p-nitrophenol degradation. *J. Water Process Eng.* **40**, 101912 (2021).
9. Khudhur, R. H. et al. Adsorption of anionic azo dye from aqueous wastewater using zeolite NaX as an efficient adsorbent. *Desalin. Water Treatm.* **306**, 245–252 (2023).
10. Khader, E. H. et al. Green nanocatalyst for the photocatalytic degradation of organic pollutants in petroleum refinery wastewater: Synthesis, characterization, and optimization. *J. Mol. Struct.* **1304**, 137688 (2024).
11. Ali, N. S. et al. Applying MCM-48 mesoporous material, equilibrium, isotherm, and mechanism for the effective adsorption of 4-nitroaniline from wastewater. *Sci. Rep.* **13**(1), 9837 (2023).
12. Habeche, F. et al. Recent advances on the preparation and catalytic applications of metal complexes supported-mesoporous silica MCM-41. *J. Inorgan. Organometall. Polym. Mater.* **30**(9), 4245–4268 (2020).
13. Deng, Y. et al. Characterization and photocatalytic evaluation of fe-loaded mesoporous MCM-41 prepared using iron and silicon sources extracted from iron ore tailing. *Waste Biomass Valoriz.* **11**(4), 1491–1498 (2020).
14. Liang, L. et al. Efficiency and mechanisms of rhodamine B degradation in Fenton-like systems based on zero-valent iron. *RSC Adv.* **10**, 28509–28515 (2020).
15. Sun, X. et al. Efficient degradation of methyl orange in water via both radical and non-radical pathways using Fe-Co bimetal-doped MCM-41 as peroxymonosulfate activator. *Chem. Eng. J.* **402**, 125881 (2020).
16. Zhang, H. et al. Catalytic degradation of chitosan by supported heteropoly acids in heterogeneous systems. *Catalysts* **10**(4), 555 (2020).
17. Zhou, S., Song, C., Kong, W., Wang, B. & Kong, Y. Effects of synergetic effect between Co and γ-Fe_2O_3 in confined silica matrix of MCM-41 on the formation of free radicals for the advanced oxidation technology. *Appl. Surf. Sci.* **527**, 146853 (2020).
18. Ali, N. S. et al. Modification of SBA-15 mesoporous silica as an active heterogeneous catalyst for the hydroisomerization and hydrocracking of n-heptane. *Heliyon* **8**(6), e09873 (2022).
19 Suyanta, S., Kuncaka, A. & Mudasir, M. Impregnation of Fe3+ into MCM-41 pores: Effect of Fe^{3+} concentration on the weight percent of Fe-frameworks and Fe-non-frameworks. *Indonesian J. Chem.* **23**, 984–996 (2023).
20. Sikorski, D., Gzyra-Jagieła, K. & Draczyński, Z. The Kinetics of Chitosan degradation in organic acid solutions. *Mar. Drugs* **19**(5), 236 (2021).
21. Ganapathy, R., & Aykaç, A. Depolymerisation of High Molecular Weight Chitosan and Its Impact on Purity and Deacetylation . *6th International Students Science Congress Proceedings Book*, 2022.
22. Yan, J. et al. Degradation of chitosan with self-resonating cavitation. *Arab. J. Chem.* **13**, 5776–5787 (2020).
23. Ramli, A., Ahmed, S. & Yusup, S. Effect of synthesis duration on the physicochemical properties of siliceous mesoporous molecular sieve (Si-MMS). *Defect Diffus. Forum* **326–328**, 647–653 (2012).
24. Savidha, R. et al. Vapor-phase isopropylation of phenol over Fe-containing Al-MCM-41 molecular sieves. *Catal. Lett.* **91**(1–2), 49–61 (2003).
25. Mikhnenko, M. D. et al. Defect structure of nanocrystalline NiO oxide stabilized by SiO_2. *Inorganics* **11**(3), 97 (2023).
26. Hachemaoui, M. et al. Metal-loaded mesoporous MCM-41 for the catalytic wet peroxide oxidation (CWPO) of acetaminophen. *Catalysts* **11**(3), 238 (2021).
27. Taherian, Z., Khataee, A. & Orooji, Y. Facile synthesis of yttria-promoted nickel catalysts supported on MgO-MCM-41 for syngas production from greenhouse gases. *Renew. Sustain. Energy Rev.* **134**, 110130 (2020).
28. Guo, Y. et al. Highly efficient nano-Fe/Cu bimetal-loaded mesoporous silica Fe/Cu-MCM-41 for the removal of Cr(VI): Kinetics, mechanism and performance. *J. Hazard. Mater.* **418**, 126344 (2021).
29. Jaramillo, L. Y., Henao, W. & Romero-Sáez, M. Synthesis and characterization of MCM-41–SBA-15 mixed-phase silica with trimodal mesoporous system and thick pore wall. *J. Porous Mater.* **27**(6), 1669–1676 (2020).
30. Huang, B. et al. Coupled surface-confinement effect and pore engineering in a single-Fe-atom catalyst for ultrafast Fenton-like reaction with high-valent iron-oxo complex oxidation. *Environ. Sci. Technol.* **57**(41), 15667–15679 (2023).
31. Farhadian, N. et al. Enhanced heterogeneous Fenton oxidation of organic pollutant via Fe-containing mesoporous silica composites: A review. *J. Mol. Liquids* **314**, 114896 (2020).
32. Castillo, R. et al. Production of MCM-41 nanoparticles with control of particle size and structural properties: Optimizing operational conditions during scale-up. *Int. J. Mol. Sci.* **21**(21), 7899 (2020).
33. Albayati, T. M. & Doyle, A. M. Encapsulated heterogeneous base catalysts onto SBA-15 nanoporous material as highly active catalysts in the transesterification of sunflower oil to biodiesel. *J. Nanoparticle Res.* **17**(1), 1–10 (2015).
34. Macková, L. et al. Infrared and Raman spectroscopy investigations in mullite-type $Bi_2(FexGa_1\text{-}x)_4O_9$ polycrystals. *Ferroelectrics* **611**(1), 239–245 (2023).
35. Yang, W. et al. Enhanced Fenton-like degradation of sulfadiazine by single atom iron materials fixed on nitrogen-doped porous carbon. *J. Colloid Interface Sci.* **597**, 56–65 (2021).
36. Guo, J. et al. MIL-100 (Fe) with mix-valence coordinatively unsaturated metal site as Fenton-like catalyst for efficiently removing tetracycline hydrochloride: Boosting Fe(III)/Fe(II) cycle by photoreduction. *Sep. Purif. Technol.* **262**, 118334 (2021).
37. Jankowska, A. et al. Catalytic performance of spherical MCM-41 modified with copper and iron as catalysts of NH_3-SCR process. *Molecules* **25**(15), 35651 (2020).
38. Alismaeel, Z. T. et al. Modification of FAU zeolite as an active heterogeneous catalyst for biodiesel production and theoretical considerations for kinetic modeling. *Adv. Powder Technol.* **33**(7), 103646 (2022).
39. Tian, S.-Q. et al. Heterogeneous catalytic ozonation of atrazine with Mn-loaded and Fe-loaded biochar. *Water Res.* **193**, 116860 (2021).
40. Ali, H. S. H. M. et al. Revealing the effect of MnO_2, activated carbon and MnO_2/activated carbon on chitosan polymer host fabricated Co NPs: Antibacterial performance and degradation of organic compounds. *Polymers* **14**(3), e4301 (2022).
41. Guo, C. et al. Optimization of heterogeneous Fenton-like process with Cu-Fe@CTS as catalyst for degradation of organic matter in leachate concentrate and degradation mechanism research. *Waste Manag.* **134**, 220–230 (2021).
42. Abd Al-Khodor, Y. A. & Albayati, T. M. Employing sodium hydroxide in desulfurization of the actual heavy crude oil: Theoretical optimization and experimental evaluation. *Process Saf. Environ. Protect.* **136**, 334–342 (2020).
43. Ren, H., Jin, X., Li, C., Li, T. & Zhou, R. Rosmarinic acid enhanced Fe(III)-mediated Fenton oxidation removal of organic pollutants at near neutral pH. *Sci. Total Environ.* **736**, 139528 (2020).

44. Huawei, G., Mou, Z., Liu, Z., Li, F. & Yang, C. Biochemical degradation of chitosan over immobilized cellulase and supported Fenton catalysts. *Catalysts* **10**(1), 124 (2020).
45. Wang, M. et al. Facile synthesis of chitosan-derived maillard reaction productions coated $CuFeO_2$ with abundant oxygen vacancies for higher Fenton-like catalytic performance. *Chemosphere* **283**, 131191 (2021).
46. Kamsuwan, T., Guntida, A., Praserthdam, P. & Jongsomjit, B. Differences in deterioration behaviors of $Cu/ZnO/Al_2O_3$ catalysts with different Cu contents toward hydrogenation of CO and CO_2. *ACS Omega* **7**(34), 25783–25797 (2022).
47. Zhou, J., Zhao, J., Jinling, Z., Zhang, T. & Liu, Z. Regeneration of catalysts deactivated by coke deposition: A review. *Chin. J. Catal.* **41**(6), 919–933 (2020).
48. Castillo, R., de la Torre, L., García-Ochoa, F. & Vallet-Regí, M. Production of MCM-41 nanoparticles with control of particle size and structural properties: Optimizing operational conditions during scale-up. *Int. J. Mol. Sci.* **21**(21), 7899 (2020).
49. Ng, E. et al. Mineralizer effects on the physicochemical and catalytic properties of AlMCM-41 mesoporous materials. *Microporous Mesoporous Mater.* **297**, 110016 (2020).
50. Santana, C. S., Bonfim, D. P. F., Cruz, I., Batista, M. S. & Fabiano, D. Fe_2O_3/MCM-41 as catalysts for methyl orange degradation by Fenton-like reactions. *Environ. Prog. Sustain. Energy* **40**(1), e13456 (2020).
51. Cao, Y. et al. Investigation of hydroxyl radical yield in an impact-jet hydraulic cavitator. *Processes* **10**(1), 124 (2022).

Author contributions

Z.Z. (Zhang Zhang) contributed to the conception and design of the study, performed the synthesis of the Fe-MCM-41 catalysts, and conducted the majority of the experiments related to the catalytic degradation of chitosan. Z.Z. also contributed to the analysis and interpretation of data, as well as drafting the manuscript. W.D. (Wuheng Dong) was responsible for conducting the X-ray diffraction (XRD) and scanning electron microscopy (SEM) analyses. W.D. also contributed to the interpretation of these results and their implications for the catalyst's structure and performance. Y.H. (Yongchun Huang) provided guidance on the overall research direction, supervised the project, and was responsible for reviewing and revising the manuscript. Y.H. also provided critical feedback on the experimental design and data analysis. All authors read and approved the final manuscript.

Funding

The fundings were provided by National Natural Science Foundation of China (Grant No. 31660472) and Guangxi Key R&D Program (Grant No. AB22035061, Research on technological innovation and industrialization demonstration of snail rice noodles noodles production).

Competing interests

The authors declare no competing interests.

Additional information

Correspondence and requests for materials should be addressed to W.D. or Y.H.

Reprints and permissions information is available at www.nature.com/reprints.

Publisher's note Springer Nature remains neutral with regard to jurisdictional claims in published maps and institutional affiliations.